ADVANCED QUANTUM TECHNOLOGIES
www.advquantumtech.com

Pressure-Driven Magneto-Topological Phase Transition in a Magnetic Weyl Semimetal

Qingqi Zeng, Hongyi Sun, Jianlei Shen, Qiushi Yao, Qian Zhang, Nana Li, Lin Jiao, Hongxiang Wei, Claudia Felser, Yonggang Wang, Qihang Liu,* and Enke Liu**

The co-occurrence of phase transitions with local and global order parameters, such as entangled magnetization and topological invariants, is attractive but seldom realized experimentally. In this study, a magneto-topological phase transition (magneto-TPT), that is, the phenomenon of magnetic materials undergoing different magnetic and topological phases during pressure loading, is investigated. By considering both out-of-plane ferromagnetic and in-plane antiferromagnetic components, it is discovered that the calculated results fit well with the experimental data. The calculation results further reveal a pristine Weyl phase with four additional pairs of Weyl nodes under low pressure, and a generally defined Z_2 topological insulator phase after the restoration of time-reversal symmetry at 40.4 GPa. The transport measurements performed at 5 K reveal that the magnetic order almost vanishes at 40.3 GPa, which is consistent with the theoretical prediction. Moreover, the present magneto-TPT involves the degeneration of a pair of crossing bands of two spin channels. Hence, all the chiral Weyl nodes annihilate with their counterparts from another spin channel, in contrast to the typical intraband annihilation of Weyl pairs in inversion-asymmetric systems. The study reveals a method for realizing diverse topological states by modulating exchange splitting by external physical knobs such as pressure in topological magnets.

1. Introduction

Topological phase transition (TPT) is a class of phase transitions beyond the Landau paradigm, which cannot be described by the spontaneous breaking of local symmetry.[1–4] As a classical case, the phase transition from a normal insulator to a topological insulator (TI) links the significantly different topological characteristics of the electronic structures of the two insulating phases.[5] By contrast, the evolution between Dirac fermions with fourfold band degeneracy and chiral Weyl fermions with twofold degeneracy can be realized between two metallic phases by breaking either the inversion symmetry or time-reversal symmetry (TRS).[5,6] In particular, the TPT achieved by changing the TRS triggers an interplay between the topology and magnetism.[7,8] When a TPT is accompanied or induced by a magnetic phase transition, the entangled degrees of freedom can be tuned cooperatively by multiple conditions (such as temperature and pressure),

---

Q. Zeng, H. Wei, E. Liu
Beijing National Laboratory for Condensed Matter Physics
Institute of Physics
Chinese Academy of Sciences
Beijing 100190, China
E-mail: ekliu@iphy.ac.cn

H. Sun
Shenzhen Institute for Quantum Science and Engineering
Southern University of Science and Technology
Shenzhen 518055, China

H. Sun
International Quantum Academy
Shenzhen 518048, China

J. Shen
Research Institute of Materials Science of Shanxi Normal University
Taiyuan 030000, China

The ORCID identification number(s) for the author(s) of this article can be found under https://doi.org/10.1002/qute.202100149

DOI: 10.1002/qute.202100149

Q. Yao, Q. Liu
Shenzhen Institute for Quantum Science and Technology and
Department of Physics
Southern University of Science and Technology (SUSTech)
Shenzhen 518055, China
E-mail: liuqh@sustech.edu.cn

Q. Zhang, N. Li, Y. Wang
Center for High Pressure Science and Technology Advanced Research
(HPSTAR)
Beijing 100094, China
E-mail: yonggang.wang@hpstar.ac.cn

L. Jiao
Department of Physics and Frederick Seitz Materials Research Laboratory
University of Illinois Urbana-Champaign
Urbana, IL 61801, USA

C. Felser
Max Planck Institute for Chemical Physics of Solids
Dresden 01069, Germany

Q. Liu
Guangdong Provincial Key Laboratory for Computational Science and
Material Design
Southern University of Science and Technology
Shenzhen 518055, China

E. Liu
Songshan Lake Materials Laboratory
Dongguan, Guangdong 523808, China

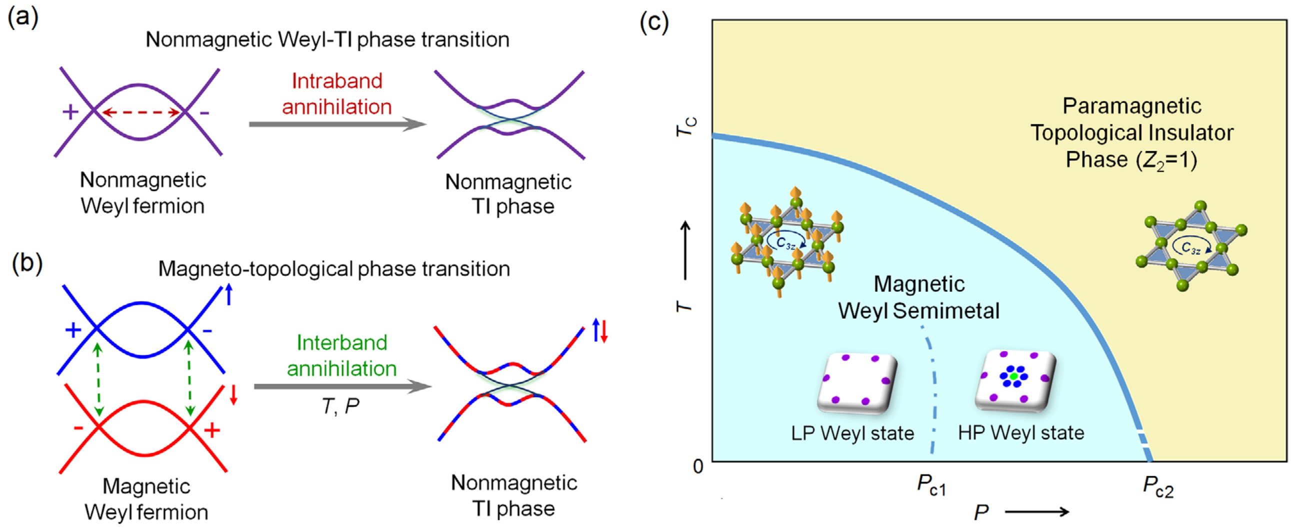

Figure 1. Topological phase transition. a) Weyl–TI TPT with intraband annihilation of chiral Weyl nodes in nonmagnetic system (in this case, inversion symmetry should be broken, e.g., TaAs). b) Weyl–TI TPT driven by temperature or pressure with interband annihilation of chiral Weyl nodes in magnetic system. Dashed arrows denote trajectory of Weyl-node annihilation (in this case, inversion symmetry is preserved, e.g., $Co_3Sn_2S_2$). For generality, we assume that phase transition preserves crystal symmetry. c) Schematic magneto-topological phase diagram of magnetic Weyl system in terms of pressure (P) and temperature (T). Specific lattice with (Weyl semimetal) and without (TI) ferromagnetic order, and low/high-pressure (LP/HP) Weyl state show example of one system undergoing different topological phases adjusted by pressure and temperature. T_C denotes Curie temperature; P_{c1} and P_{c2} denote potential critical pressures of first and second TPTs, respectively.

which is attractive for the realization of various topological quasiparticles[9,10] and applications of novel topological spintronics.[11–14]

Here, we considered the emerging Weyl–TI phase transition, involving two distinct topological nontrivial phases as well as a metal–insulator transition. By preserving the TRS, the chiral Weyl nodes can annihilate in pairs with each other upon phase transition (see **Figure 1**a). However, it is difficult to identify a generic tuning parameter to trigger the TI phase. By contrast, when magnetism is involved, the magnetic order naturally performs as an order parameter driving the material to different topological phases during spontaneous magnetization.[6,15] In addition, such magneto-TPT will reveal a new type of Weyl-node annihilation. As shown in Figure 1b, the Weyl nodes from one spin channel can meet and annihilate with the corresponding band crossings of the other spin channel. It is desirable for the magnetic Weyl system to become an Z_2 TI if the band inversion persists when the magnetism is completely suppressed, as schematically shown in Figure 1c. In addition, TPT between different Weyl states may be induced by pressure as band structure can significantly vary with high-pressure loading.[5,16,17] Hence, different topological phases may be obtained by adjusting well-controlled parameters such as pressure and temperature (see Figure 1c).

However, realizing such magnetism-involved TPT is technically challenging and yet to be validated experimentally, because it highlights the essence of intrinsic topological magnets, which are rarely investigated. Recently, TPT around the Curie temperature of $Co_3Sn_2S_2$ is revealed by temperature-dependent angle-resolved photoemission spectroscopy (ARPES) studies,[18–20] indicating that the transition from Weyl semimetal to TI in $Co_3Sn_2S_2$ can be driven by temperature. Compared with the thermal effect, which destroys the magnetic order at relatively high temperatures, pressure can suppress the magnetism at low temperatures; hence, the intrinsic physical behaviors should be investigated more comprehensively.

In this study, we focus on the TPT and apply high pressure to investigate the evolution of topological states in a $Co_3Sn_2S_2$ Weyl magnet. Since its discovery,[21–24] significant topological characteristics, including giant anomalous Hall effects (AHEs),[21,22] anomalous Nernst effects,[25,26] surface Fermi arcs,[23,24] chiral edge states,[27,28] giant magneto-optical Kerr effects,[29] spin-orbit polaron,[30] low-resistance state/exceptional Hall component,[31] spin wave gap,[32] and anisotropic magnetoelastic response[33] have been observed in $Co_3Sn_2S_2$, rendering it an ideal platform for TPTs with TRS breaking and restoration. Recently, pressure studies have been performed to adjust the giant AHE of $Co_3Sn_2S_2$, where it is discovered that the intrinsic mechanism-dominated AHE decreased during pressure loading.[34,35] Pressure can suppress ferromagnetism and reduce the distance between Weyl nodes with opposite chirality. However, the potential TPT as well as the evolution of the topological state upon phase transition remains unaddressed.

Combining transport measurements and first-principles calculations, it is revealed that by increasing pressure, the out-of-plane ferromagnetic (FM) ordering is suppressed, whereas in-plane antiferromagnetic (AFM) components emerged in $Co_3Sn_2S_2$, with a concurrent decrease in the intrinsic anomalous Hall conductivity (AHC). From ambient pressure up to ≈40 GPa, the system evolves from a low-pressure Weyl phase to a high-pressure Weyl phase, and finally to a general TI phase with Pauli paramagnetism (PM), accompanied by vanishing spin polarization and AHC. Unlike the pressure-induced TPT in nonmagnetic materials, where the pressure triggers band inversion,[16,36] spontaneous magnetism serves as a pivot that promotes the TPT

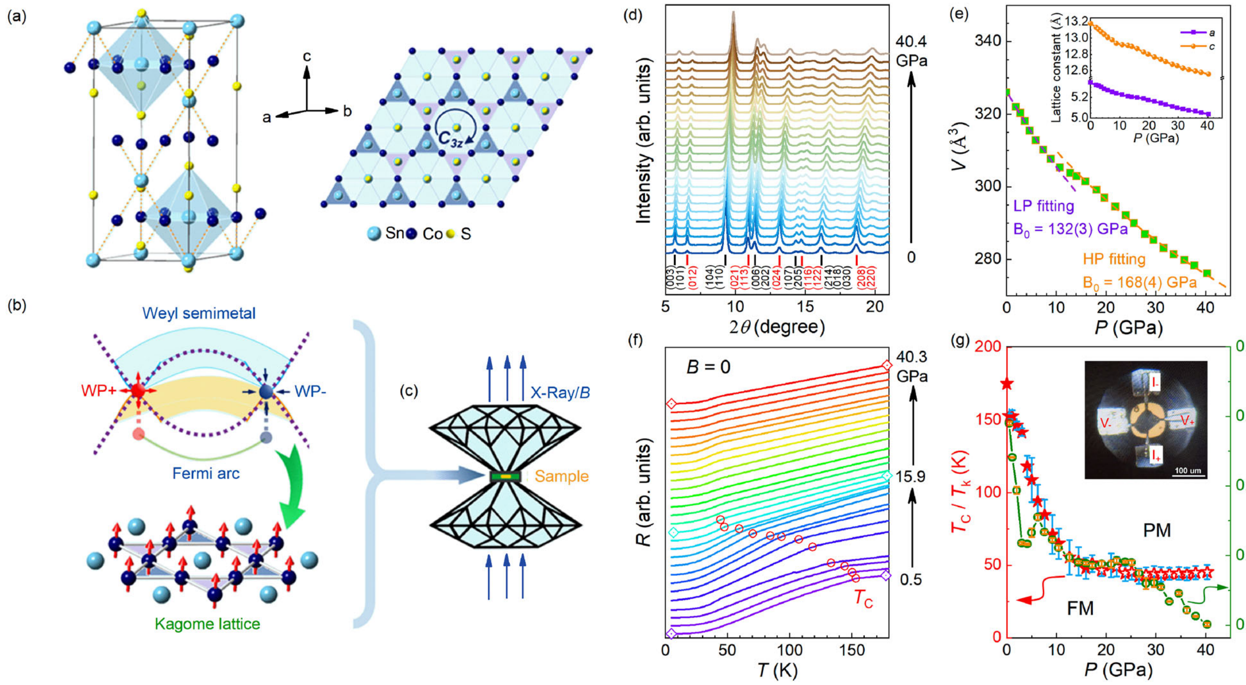

Figure 2. Crystal structure, topological state, pressure-dependent X-ray diffraction and electric resistivity. a) Hexagonal unit cell of $Co_3Sn_2S_2$. Kagome lattice formed by Co atoms are depicted in right panel of (a) and lower panel of (b) in different perspectives. Magnetic moments in Co sites along *c*-axis direction are indicated by red arrows. A sketch of band inversion, Fermi arc, and Weyl nodes on Co-atom Kagome lattice is shown in upper panel of (b). c) Sketch of high-pressure experimental configuration. d) X-ray diffraction patterns of $Co_3Sn_2S_2$ under different pressures. e) Pressure dependence of unit cell volume in rhombohedral space group *R*-3*m*. Purple and orange dash lines show fitting results based on the equation of state. Inset shows pressure dependence of lattice parameters. f) Temperature dependence of resistance in arbitrary units under different pressures. Diamond symbols provide visual guidance, through which curves under 0.5, 15.9, and 40.3 GPa can be visualized clearly. g) Pressure dependences of Curie temperature (solid star), kink temperature (open star), and coercive field. "PM" and "FM" indicate paramagnetic and ferromagnetic states, respectively. Inset shows sample and configuration of Hall measurements.

in response to pressure. Furthermore, because our magneto-TPT involves the bands of two spin channels becoming degenerate by restoring the TRS, all of the Weyl nodes annihilate with their counterparts from another spin channel in higher conduction bands. Hence, a magneto-TPT with a new mechanism of Weyl-node annihilation is indicated in this topological magnet.

2. Results and Discussion

The Shandite $Co_3Sn_2S_2$ adopts a rhombohedral structure with an *R*-3*m* space group. The unit cell in a hexagonal representation is shown in **Figure 2**a, in which one Sn atom is at the center of the Kagome lattice formed by Co atoms, whereas S and the remaining Sn atoms are located between the Co_3Sn Kagome layers. $Co_3Sn_2S_2$ is known to be an itinerant ferromagnet with a magnetic moment of 0.29 μ_B per Co atom,[21,37] with the measured easy axis along the *c*-axis,[38] as indicated by the red arrows in Figure 2b. A schematic sketch of the band inversion of Co orbitals on the Kagome lattice is shown in Figure 2b. The red and blue spots show the Weyl nodes with opposite chirality, serving as a monopole sink and source of the Berry curvature in momentum space.[21] The surface Fermi arc connects the projection of the two Weyl nodes.[21,23,24] All these topological characteristics exist in the Co atom Kagome lattice in $Co_3Sn_2S_2$. Pressure-dependent studies regarding $Co_3Sn_2S_2$ were conducted using a Be/Cu diamond anvil cell with X-ray and magnetic field passing through the diamond windows (as shown in Figure 2c). The $Co_3Sn_2S_2$ samples used in this study were single-crystalline microflakes (see the details in Experimental Section and Note S1, Supporting Information). For X-ray diffraction (XRD) measurement, the sample was well-grinded and pressed to be a pellet. Figure 2d shows the XRD patterns of $Co_3Sn_2S_2$ under pressure, from which no obvious structural phase transition was observed up to 40 GPa. All the XRD data were refined with the space group *R*-3*m* (as shown in Figure 2e and Note S2, Supporting Information). The lattice parameters *a* and *c*, along with the cell volume *V*, decrease with increasing pressure, which is similarly observed in a previous report.[34] Both the low-pressure region (0–10 GPa) and high-pressure region (15–40 GPa) can be well fitted using the third-order Birch–Murnaghan equation of state.[39] Between 10 and 15 GPa, the compression of the unit cell appeases abating, which may be due to a subtle electronic transition.

We measured the temperature dependence of the longitudinal resistance (*R*–*T*) of $Co_3Sn_2S_2$ under high pressures, as shown in Figure 2f. All first-order differentials of the *R*–*T* curves were further recorded, and the abrupt changes (kink point on *R*–*T* curves) were determined to be the Curie temperature T_C (see Note S3, Supporting Information for details). The T_C decreases with increasing pressure (the data from 0.5 to 17 GPa are shown as solid symbols in Figure 2g), similar to observations in previous studies.[34,35,40] Kinks emerge at about 45 K and remain almost

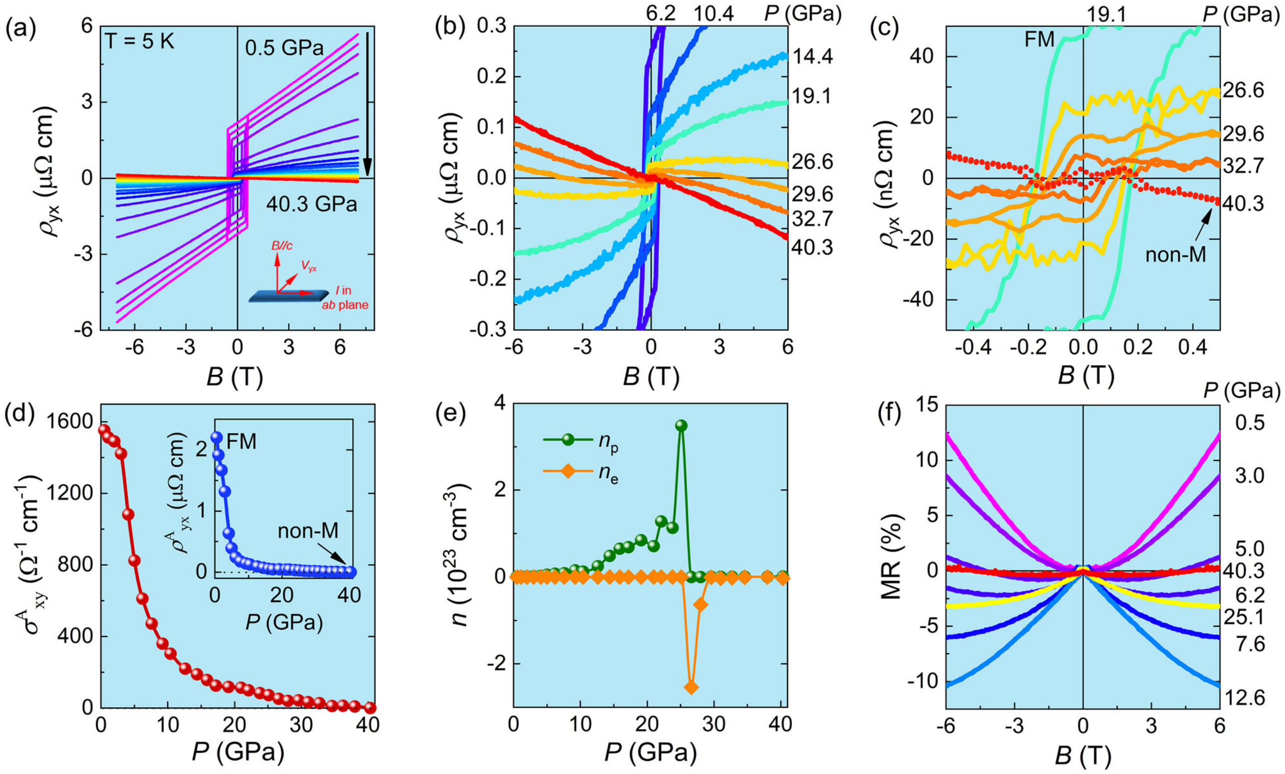

Figure 3. Hall effect, carrier, and MR under pressure. a–c) Magnetic field dependence of Hall resistivity under different pressures. b,c) Enlarged scales of (a). d) Pressure dependence of anomalous Hall conductivity. Inset shows pressure dependence of anomalous Hall resistivity. e) Pressure dependences of carrier concentrations. Subscripts p and e denote holes and electrons, respectively, in two-band analysis. f) Pressure dependence of MR at 5 K. At low pressures, system shows magnetic Weyl state with large MR; at high pressures, system becomes nonmagnetic with small MRs.

unchanged above 17 GPa (shown as open symbols in Figure 2g). Based on an analysis of the coercive field (illustrated below), the magnetism in this system is indeed suppressed by high pressures. Hence, the unchanged kink is not attributed to T_C above 17 GPa in this study. Other transitions may occur in this system and results in an unchanged kink temperature (T_k) above 17 GPa.

As the coercive field in the magnetization loop can indicate the FM order, we further analyzed the coercive field (H_c) extracted from the Hall data measured at 5 K (see Figure 2g and Note S3.3, Supporting Information for details). The FM order changes only slightly between 17 and 25 GPa, but decreases rapidly above 26 GPa and almost vanishes at about 40 GPa. Hence, it can be concluded that the itinerant FM order approaches near nonmagnetic state, or in other words, the Pauli PM,[41] above the critical pressure of 40 GPa.

Figure 3a-c shows the Hall data under different pressures. As shown in Figure 3a, the data indicate a linear, positive-slope behavior for the high-field normal Hall part. This shows the dominance of hole carriers in this system. It is observed that the transverse resistivity at zero-field $\rho_{yx}(0)$, that is, the anomalous Hall resistivity, decreases rapidly with increasing pressure, which is also depicted in the inset of Figure 3d. Based on an amplified scale (Figure 3b), the Hall curves show positive slopes below 26.6 GPa, above which the slope changes to negative, indicating a switch in the dominant carrier type. In two previous reports, the switch of carrier type is either observed at a lower pressure[34] or not observed.[35] The abovementioned difference might be due to variations in the samples used. Meanwhile, the characteristics of the loop hysteresis become more faint gradually (Figure 3c), leaving an almost linear response of the normal Hall effect at high pressures. At 40 GPa, both the AHE and H_c approach zero (see Figures 3d and 2g). Correspondingly, the AHC decreases remarkably from 1550 Ω^{-1} cm^{-1} to almost zero with increasing pressure up to 40 GPa (Figure 3d), indicating that the FM order almost vanishes under high pressures. In a previous report,[34] linear extrapolation of experimental results indicated that the FM order is suppressed at 22 GPa. However, nonlinear reduction of magnetic order and higher critical pressure can be concluded from our experimental data (up to 40.3 GPa).

Because the Hall curves show a nonlinear behavior in the high-field region between the pressures of 10 and 30 GPa (Figure 3b), we employed the two-band model[42,43] for all the Hall data measured at 5 K (see Experimental Section and Note S3.4, Supporting Information for details) to obtain the carrier concentrations (shown in Figure 3e). During pressure loading, a notable switch in carrier type is evident at 25–27 GPa. Below 25.1 GPa, the transport behavior is dominated by holes, with the hole concentration increasing from 8.5×10^{20} cm^{-3} ($P = 0.5$ GPa) to 3.5×10^{23} cm^{-3} ($P = 25.1$ GPa), that is, by three orders of magnitude. Above 26.6 GPa, the dominant carrier switches rapidly to electron. The electron concentration also shows a maximum value of 2.5×10^{23} cm^{-3} ($P = 26.6$ GPa) and decreases to 2.9×10^{21} cm^{-3} ($P = 40.3$ GPa), that is, by two orders of magnitude, resulting in a relatively high concentration of electrons. It can be known that the Fermi surfaces of the electrons and holes increase simultaneously, and a compensation between the two carriers with high concentrations occurs at a pressure of about 26 GPa. A synchronous abrupt decrease in H_c occurs at about 26 GPa (Figure 2g); therefore, a strong correlation may exist between the evolution of the electronic structure and the spin splitting under pressure.

Figure 3f shows the pressure dependence of the magnetoresistance (MR) (see Note S3.5, Supporting Information for all data). Below 3.0 GPa, a positive MR is observed, which is consistent with that of bulk samples under zero pressure.[21] With increasing pressure, the MR decreases rapidly and finally exhibited negative values above 6.2 GPa, indicating a maximum value at about 12.6 GPa. Magnetic materials typically exhibits a negative MR owing to spin-related scattering.[44] Hence, during loading, competition exists between the positive MR from the ordinary MR and the negative MR from spin-related scattering. Above 26 GPa, the negative MR decays as the ferromagnetism weakens above this pressure (see also Figure 2g).

Additionally, pronounced kinks are observed at about 3 GPa in both the pressure dependence of T_C and H_c as well as AHC curves, after which the values of all the abovementioned magnetic-related parameters decreases rapidly. Based on the magnetic measurements (see Note S1, Supporting Information) of $Co_3Sn_2S_2$ at ambient pressure, a magnetic transition occurs below T_C, which is consistent with previous studies.[21,40,45,46] The pronounced difference between the zero-field-cooling and field-cooling curves indicates that magnetic interactions other than out-of-plane FM interactions[21,45,46] may exist. An earlier report showed that in-plane AFM components emerged in $Co_3Sn_2S_2$ above 90 K at ambient pressure. Furthermore, high pressure supports this magnetic phase to lower temperatures.[40] Hence, one possible reason for the rapid decrease at 3 GPa is the in-plane AFM interaction. In-plane AFM components may appear, which will result in a much lower AHC, as the out-of-plane ferromagnetic order is crucial to the topological transport properties in this system.[21,22,40]

Nevertheless, we stress that regardless of the magnetic order variance during the pressure loading, the investigated sample approaches a near-nonmagnetic state above 40 GPa, as indicated by the almost vanished H_c and AHC. Hence, one can expect a magnetic phase transition from the FM state to the PM state above 40 GPa at low temperatures in $Co_3Sn_2S_2$. This implies that the TRS-broken Weyl fermions would annihilate at high pressure due to the restoration of the TRS in a space-inversion-protected system. Hence, a TPT can be expected concurrent with the magnetic phase transition.

To explore the possible pressure-induced magneto-TPTs, we investigated the magnetic and electronic properties of $Co_3Sn_2S_2$ under pressure using density functional theory (DFT) calculations (see details in Experimental Section). DFT results show that under ambient pressure, $Co_3Sn_2S_2$ is an FM nodal-line semimetal without spin-orbit coupling (SOC),[21,22,47] where six nodal rings in the first Brillouin zone near the Fermi level are formed by band inversion between two spin-up bands. When SOC is considered, the band structure remains similar to the one without SOC, except that the SOC lifted the band crossings along the U–L–Γ *k*-path. The gaped band crosses are along the U–L and L–Γ paths (red bands in **Figure 4**d and see Note S4.1, Supporting Information). Similar crosses are observed in the conduction bands, which are at a higher energy for the spin-down-dominant channel (blue bands in Figure 4d).

Based on the analyses above regarding the possible in-plane AFM components, we performed two types of calculations. One type only considers out-of-plane linear FM components, whereas the other includes in-plane AFM components. The results indicate that the latter type is more consistent with the experimental results. For the in-plane AFM components, six magnetic structures with different in-plane AFM components were considered, two of which are shown in Figure 4a (more details are provided in Note S4.2, Supporting Information). The calculated AHC with total moments tilting 45° away from the *z*-axis and in-plane component orders of m2 and m3 are shown in Figure 4c (right axis). Although the tilted angle should vary as pressure increases, our calculated results with fixed angle show the same trend as the experimental data. Both experimental and theoretical (Figure 4c) results show that the AHC decreases rapidly with increasing pressure. The calculated total moments under the involved magnetic configurations are shown in Figure 4c. The moment decreases once the pressure is loaded. Finally, the local moment of $Co_3Sn_2S_2$ vanishes under a pressure of about $P_{c2} = 40.4$ GPa. Meanwhile, as show in Figure 4e, the bands of the spin-up and spin-down channels degenerate at 40.4 GPa (see also Note S4.3, Supporting Information), resulting in a zero local moment (no spin polarization) on the Co atoms and hence the TRS restoration of the system. In optical spectra research pertaining to $Co_3Sn_2S_2$, the temperature-dependent optical conductivity shows that spin-band splitting is reduced as exchange interactions decrease when the temperature approaches T_C. This results in the reduction in both the Berry curvature and AHC.[48] Hence, it can be concluded that the evolution of the AHC directly correlates with the vanishing of ferromagnetism as pressure or temperature increases in $Co_3Sn_2S_2$.

To confirm that the Pauli PM is a stable magnetic state under high pressures, we performed further calculations based on six magnetic structures. All results indicate a consistent convergence to the Pauli PM for all considered AFM components under a high pressure of 40.4 GPa. Moreover, all the AFM systems possess a higher energy (Figure 4b) compared with the PM when the AFM structures were constrained (see also Note S4.4, Supporting Information). These results indicate TRS restoration under 40.4 GPa. Hence, high pressure can serve as an experimentally adjustable parameter for switching the itinerant FM system to a TRS-preserved Pauli PM phase. In this case, TPTs may occur concurrently.

Next, we discuss the expected pressure-induced TPT. At relatively low pressures, we observe a Weyl phase transition with two additional types of Weyl nodes (additional four pairs, denoted as W2 and W3) near pressure $P_{c1} = 20$ GPa. In a previous report,[34] similar transition was reported at 8.46 GPa. The discordant critical pressure can be attributed to the different considered magnetic configuration. Only FM is considered in abovementioned reference, whereas out-of-plane FM and in-plane AFM components are included in this study. A more well-fitted pressure-dependent AHC in our study shows the necessity of including the AFM components. The position evolution of these Weyl nodes is shown in Figure 4f (for W1) and 4g (for W2 and W3). Our DFT results further reveal the unique an-

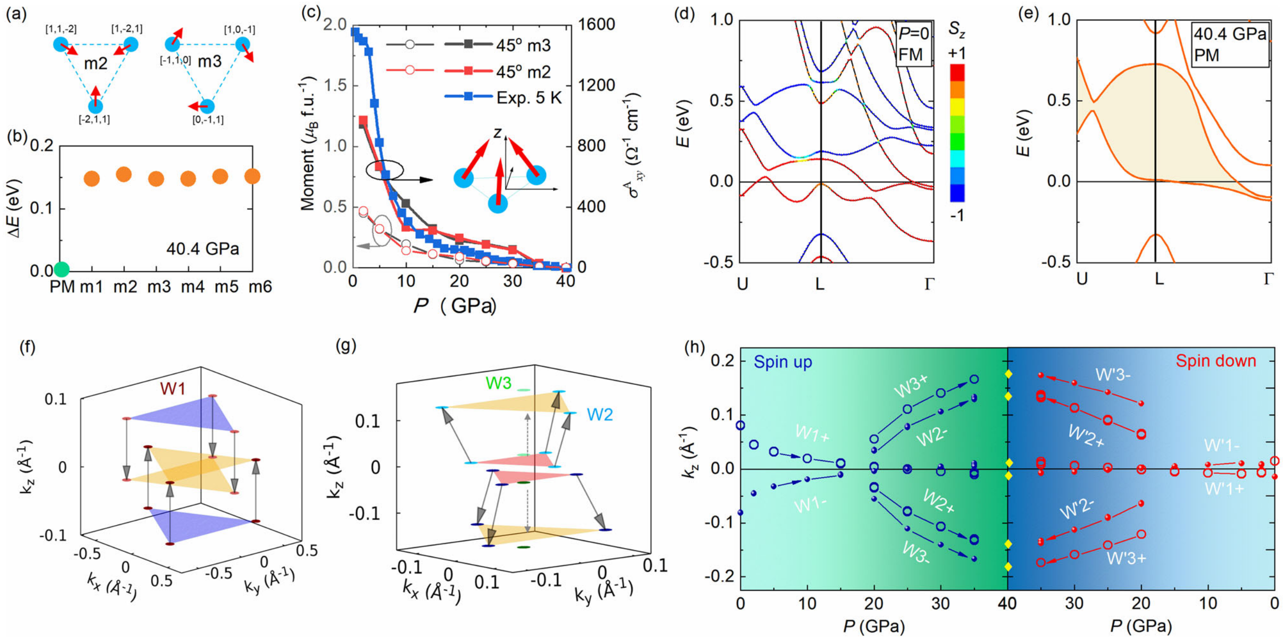

Figure 4. Theoretical calculations of magnetic and topological properties under pressure. a) Two in-plane AFM components considered. b) Energy difference between zero-moment PM state and six constrained in-plane AFM components (as shown in Note S4.2, Supporting Information) with fixed moment directions and values (details in Note S4.4, Supporting Information). Energy of zero-moment PM state is set to zero. c) Pressure dependences of magnetic moment and AHC under two considered in-plane AFM m2 (red) and m3 (grey) configurations with fixed directions and relaxed values. Blue curve shows measured pressure dependence of AHC. The inset sketches the tilted moments with out-of-plane FM and in-plane AFM components. Angle between moments and *z*-axis should be varied during pressure loading. Electronic structures of d) 0 and e) 40.4 GPa with high-symmetry paths in Brillouin zone. Calculations were performed based on configuration of out-of-plane linear ferromagnetic and PM structures, separately. SOC is included, and color scale in (d) denotes projection of spin onto *z*-axis. Weyl nodes annihilate during phase transition at P_{c2} = 40.4 GPa. Hence, with an inverted band gap, a pressure-induced TI phase emerges under both inversion symmetry and TRS. f,g) Position evolutions of Weyl nodes W1 and W2 and W3 in spin-up channel. W1 exists during entire loading process, whereas W2 and W3 appear above 20 GPa. h) k_z-direction trajectory of Weyl nodes from spin-up channel (blue color) and their counterparts from spin-down channel (red color), indicating interband annihilation process near P_{c2} = 40.4 GPa. Circles and dots denote Weyl nodes with chirality = +1 and −1, respectively.

nihilation mechanism of magneto-TPTs. At high pressures, all the W1, W2, and W3 Weyl nodes (from the spin-up channel) move away from their partners with opposite chirality (see Figure 4h for the k_z-trajectory and Note S4.5, Supporting Information for k_x- and k_y-trajectories), indicating that they do not annihilate intraband with each other at the magnetic transition point at 40.4 GPa. Instead, W1, W2, and W3 meet with the corresponding band crossings W'1, W'2, and W'3 for the spin-down channel at 40.4 GPa. Therefore, the Weyl semimetal phase undergoes TPT via interband annihilation. This is in stark contrast to nonmagnetic Weyl semimetals such as TaAs, in which the Weyl nodes with opposite chirality annihilate intraband with each other. Recently, a TPT around *Tc* in $Co_3Sn_2S_2$ was revealed in temperature-dependent ARPES studies.[18–20] Furthermore, it is indicated that the TPT in $Co_3Sn_2S_2$ can be promoted by both temperature and pressure.

In the following, we provide more details regarding the TPT. Figure 4e shows the band dispersions of PM $Co_3Sn_2S_2$ under a pressure of 40.4 GPa. The annihilation of Weyl nodes is accompanied by the opening of a band gap (filled region). Therefore, provided that band inversion persists, a curved Fermi level can be defined within such a gap region and hence the corresponding topological invariant can be calculated. Our calculation using the Fu-Kane formula yielded a nontrivial Z_2 = 1, indicating that such a high-pressure state is a "general TI phase" (where we relax the restriction of "a global band gap" to "a continuous band gap" between the highest valence band and the lowest conduction band). This implies that the pressure up to 40.4 GPa can completely suppress the ground state of itinerant ferromagnetism and hence induce a TPT from a magnetic Weyl semimetal phase to a nonmagnetic TI phase with the annihilation of Weyl fermions in $Co_3Sn_2S_2$.

It is known that a strict TI involves two important aspects, that is, the TRS and Fermi level inside the inverted band gap. However, in some itinerant ferromagnetism system, such as $Co_3Sn_2S_2$, a global band gap should not be expected. When a high pressure or temperature results in a Pauli PM phase,[41] the TRS is preserved both globally and locally. Together with inversion symmetry, each energy band is at least double degenerate. Hence, the time-reversal symmetric $Co_3Sn_2S_2$ must contain a half-filled band, as the total number of electrons in its unit cell is an odd number. By contrast, when a magnetic Weyl semimetal dominated by local moments is adjusted to a PM phase, the TRS is preserved globally but broken locally. One example is the recently discovered magnetic TI $MnBi_2Te_4$,[49] whose FM phase is predicted to be a magnetic Weyl semimetal[50,51] and PM phase is verified to be a 3D TI owing to the severe disorder of local moments.[52] Since the FM phase is not the ground state in

$MnBi_2Te_4$, the TPT from magnetic Weyl semimetal to the TI is barely observed in the absence of a magnetic field. Hence, we herein propose a method to realize a magneto-TPT by adjusting individual parameters, such as pressure or temperature. Whereas a pressure-induced TPT can occur at extremely low temperatures, one can expect less thermal-related effects and a more intrinsic transition process.

To summarize, a magneto-TPT from the ferromagnetic Weyl phase to the paramagnetic TI phase caused by external pressure was investigated in a magnetic Weyl semimetal $Co_3Sn_2S_2$. By considering in-plane AFM components, the rapid decrease of AHC above 3 GPa in experiments can be well fitted by simulations. Based on this magnetic configuration, calculated results further show two TPTs in this system. Pressure drives the ground FM Weyl state to transform to a new in-plane AFM and out-of-plane FM state with additional Weyl nodes around 20 GPa, and finally to the TRS-preserved Z_2 TI phase above 40 GPa. This coupling of magnetic order and TPT will enable more sophisticated topological quantum phenomena in the future, thereby promoting investigations into magneto-TPTs in other material systems, for example, those involving an intrinsic global gap in the nonmagnetic phase. We expect these evolutions of topological states in magnetic Weyl semimetals to expand the investigations of topological electronic states that manifest exotic quantum states and suggest advanced topological electronics.

3. Experimental Section

Growth and Characterizations of Single-Crystalline Microflakes: All chemicals were of reagent-grade quality and used as received from commercial sources. The single crystal microflakes of $Co_3Sn_2S_2$ were grown by chemical vapor transport (CVT) method. The polycrystalline powders of $Co_3Sn_2S_2$ as source material and I_2 as a transport agent were used. In order to reduce the nucleation points during the growth process, a reverse temperature gradient was utilized before the crystal growth. The temperatures of the source and growth zones were first stabilized at 800 and 900 °C, respectively, for 48 h. Then the sample growth was initiated by setting the source and growth zones at 850 and 800 °C, respectively, for 2 weeks. Hexagonal single-crystalline microflakes with dimension of 2–4 mm and thickness of around 10 μm were obtained. The magnetism, electric resistivity, and chemical composition of the microflakes were characterized, which confirmed the high-quality $Co_3Sn_2S_2$ samples. More details can be found in Note S1, Supporting Information.

In Situ High-Pressure X-Ray Diffraction Measurements: For the in situ high-pressure XRD measurements, a symmetrical DAC with a pair of 400 μm diameter culet sized anvils was employed to generate high pressure. An Re gasket was pre-indented to 40 μm in thickness followed by laser-drilling to form a 150 μm diameter hole serving as the sample chamber. A well-grinded and pressed $Co_3Sn_2S_2$ pellet was loaded in the sample chamber. Silicone oil was used as the pressure-transmitting medium and the pressure was calibrated by using the ruby fluorescence shift at room temperature. The in situ synchrotron XRD experiments were carried out at the 4W1 High Pressure Station in the Beijing Synchrotron Radiation Facility (BSRF). The diffraction data were recorded by a Pilatus detector, and high-purity CeO_2 powder was used for calibration.

High-Pressure Electric Transport Measurements: The high-pressure electric transport measurements were conducted on a $Co_3Sn_2S_2$ single crystal using the Quantum Design PPMS-9. A Be/Cu DAC with 300 μm culet anvils and a c-BN gasket were used. Four Pt wires were adhered to a $Co_3Sn_2S_2$ single crystal using the silver epoxy. Silicone oil was used as the pressure-transmitting medium and the pressure was calibrated by using the ruby fluorescence shift at room temperature. For the Hall measurements, magnetic fields were along the crystallographic *c* direction.

Analysis of Electric Transport: The longitudinal resistivity was calculated by van der Pauw method[53] (see Note S3.1, Supporting Information for details). In practical measurements, there are weak transverse voltage drops on longitudinal data and longitudinal voltage drops on transverse data due to the mismatch of the electrodes. In order to obtain the accurate resistivity data, the procedure of (anti-)symmetrization was applied to extract the odd (even) parts of the observed signal. As the Hall curves show an observable nonlinear behavior in high magnetic field region between 10 and 30 GPa, indicating the existence of two types of carriers (electrons and holes), two-band model analysis was therefore employed[43,54] after removing the AHE component. The details including carrier concentration and mobility can be found in Note S3.4, Supporting Information.

Density Functional Theory Calculations: DFT method was applied by using the projector-augmented wave (PAW) pseudopotentials with the exchange-correlation of Perdew–Burke–Ernzerhof revised for solids (PBEsol) form and GGA approach as implemented in the Vienna ab initio Simulation Package (VASP).[55–58] For each pressure case, the crystal lattice and atomic position were fully relaxed until the atomic force on each atom was less than 10^{-2} eV Å^{-1}. The energy cutoff and K-mesh sampling were set to 500 eV and 15 × 15 × 15, respectively. Wannier representations were constructed by projecting the Bloch states from the DFT calculations of bulk materials onto Co-3*d*, S-3*p*, Sn-5*s*, and Sn-5*p* orbitals. The AHC was expressed as the sum of the Berry curvature over all the occupied bands $\sigma_{xy}^{\mathrm{AH}} = \frac{e^2}{\hbar}\frac{1}{N_k\Omega_c}\sum_k\sum_n f_{nk}\Omega_n^z(k)$, where N_k, Ω_c, f_{nk}, and $\Omega_n^z(k)$ are total k-points number in BZ, volume of primitive cell, Femi distribution function, and Berry curvature, respectively.[59] The locations and chiralities of Weyl nodes, AHC (with a 200 × 200 × 200 K-mesh), Z_2 number, and band/energy-occupied Berry curvatures were all calculated in the tight-binding models constructed by these Wannier representations,[60–62] as implemented in the Wannier Tools package.[8]

Supporting Information

Supporting Information is available from the Wiley Online Library or from the author.

Acknowledgements

Q.Z. and H.S. contributed equally to this work. This study was supported by Fundamental Science Center of the National Natural Science Foundation of China (No. 52088101), Beijing Natural Science Foundation (No. Z190009), National Natural Science Foundation of China (Nos. 11974394, 12174426), National Key R&D Program of China (Nos. 2019YFA0704900 and 2020YFA0308900), the Strategic Priority Research Program (B) of the Chinese Academy of Sciences (CAS) (XDB33000000), the Key Research Program of CAS (No. ZDRW-CN-2021-3), and the Scientific Instrument Developing Project of CAS (No. ZDKYYQ20210003). Work at SUSTech was supported by Guangdong Innovative and Entrepreneurial Research Team Program (No. 2017ZT07C062), the Guangdong Provincial Key Laboratory of Computational Science and Material Design (No. 2019B030301001), and Center for Computational Science and Engineering of Southern University of Science and Technology. Work at HPSTAR was supported by the Major Program of the National Natural Science Foundation of China (22090041).

Conflict of Interest

The authors declare no conflict of interest.

Data Availability Statement

The data that support the findings of this study are available in the Supporting Information of this article.

Keywords

high pressure, magnetic Weyl semimetals, topological phase transition

Received: November 24, 2021
Revised: January 11, 2022
Published online:

---

[1] M. Continentino, *Quantum Scaling in Many-Body Systems: An Approach to Quantum Phase Transitions*, 2nd ed., Cambridge University Press, Cambridge **2017**.

[2] V. L. Berezinsky, *Sov. Phys. JETP* **1971**, *32*, 493.

[3] J. M. Kosterlitz, D. J. Thouless, *J. Phys. C: Solid State Phys.* **1973**, *6*, 1181.

[4] Q. Faure, S. Takayoshi, S. Petit, V. Simonet, S. Raymond, L.-P. Regnault, M. Boehm, J. S. White, M. Månsson, C. Rüegg, P. Lejay, B. Canals, T. Lorenz, S. C. Furuya, T. Giamarchi, B. Grenier, *Nat. Phys.* **2018**, *14*, 716.

[5] N. P. Armitage, E. J. Mele, A. Vishwanath, *Rev. Mod. Phys.* **2018**, *90*, 015001.

[6] B. Yan, C. Felser, *Annu. Rev. Condens. Matter Phys.* **2017**, *8*, 337.

[7] W. L. Liu, X. Zhang, S. M. Nie, Z. T. Liu, X. Y. Sun, H. Y. Wang, J. Y. Ding, L. Sun, Z. Huang, H. Su, Y. C. Yang, Z. C. Jiang, X. L. Lu, J. S. Liu, Z. H. Liu, S. L. Zhang, H. M. Weng, Y. F. Guo, Z. J. Wang, D. W. Shen, Z. Liu, arXiv:2103.04658v1, **2021**.

[8] Q. Wu, S. Zhang, H.-F. Song, M. Troyer, A. A. Soluyanov, *Comput. Phys. Commun.* **2018**, *224*, 405.

[9] J. Wang, S.-C. Zhang, *Nat. Mater.* **2017**, *16*, 1062.

[10] B. Keimer, J. E. Moore, *Nat. Phys.* **2017**, *13*, 1045.

[11] Y. Tokura, M. Kawasaki, N. Nagaosa, *Nat. Phys.* **2017**, *13*, 1056.

[12] D. N. Basov, R. D. Averitt, D. Hsieh, *Nat. Mater.* **2017**, *16*, 1077.

[13] A. Soumyanarayanan, N. Reyren, A. Fert, C. Panagopoulos, *Nature* **2016**, *539*, 509.

[14] A. R. Mellnik, J. S. Lee, A. Richardella, J. L. Grab, P. J. Mintun, M. H. Fischer, A. Vaezi, A. Manchon, E. A. Kim, N. Samarth, D. C. Ralph, *Nature* **2014**, *511*, 449.

[15] P. Wang, J. Ge, J. Li, Y. Liu, Y. Xu, J. Wang, *The Innovation* **2021**, *2*, 100098.

[16] M. S. Bahramy, B. J. Yang, R. Arita, N. Nagaosa, *Nat. Commun.* **2012**, *3*, 679.

[17] X. Wang, Z. Li, M. Zhang, T. Hou, J. Zhao, L. Li, A. Rahman, Z. Xu, J. Gong, Z. Chi, R. Dai, Z. Wang, Z. Qiao, Z. Zhang, *Phys. Rev. B* **2019**, *100*, 014407.

[18] A. Rossi, V. Ivanov, S. Sreedhar, A. L. Gross, Z. Shen, E. Rotenberg, A. Bostwick, C. Jozwiak, V. Taufour, S. Y. Savrasov, I. M. Vishik, *Phys. Rev. B* **2021**, *104*, 155115.

[19] I. Belopolski, T. A. Cochran, X. Liu, Z.-J. Cheng, X. P. Yang, Z. Guguchia, S. S. Tsirkin, J.-X. Yin, P. Vir, G. S. Thakur, S. S. Zhang, J. Zhang, K. Kaznatcheev, G. Cheng, G. Chang, D. Multer, N. Shumiya, M. Litskevich, E. Vescovo, T. K. Kim, C. Cacho, N. Yao, C. Felser, T. Neupert, M. Z. Hasan, *Phys. Rev. Lett.* **2021**, *127*, 256403.

[20] D. F. Liu, Q. N. Xu, E. K. Liu, J. L. Shen, C. C. Le, Y. W. Li, D. Pei, A. J. Liang, P. Dudin, T. K. Kim, C. Cacho, Y. F. Xu, Y. Sun, L. X. Yang, Z. K. Liu, C. Felser, S. S. P. Parkin, Y. L. Chen, *Phys. Rev. B* **2021**, *104*, 205140.

[21] E. K. Liu, Y. Sun, N. Kumar, L. Muchler, A. Sun, L. Jiao, S. Y. Yang, D. Liu, A. Liang, Q. Xu, J. Kroder, V. Suss, H. Borrmann, C. Shekhar, Z. Wang, C. Xi, W. Wang, W. Schnelle, S. Wirth, Y. Chen, S. T. B. Goennenwein, C. Felser, *Nat. Phys.* **2018**, *14*, 1125.

[22] Q. Wang, Y. Xu, R. Lou, Z. Liu, M. Li, Y. Huang, D. Shen, H. Weng, S. Wang, H. Lei, *Nat. Commun.* **2018**, *9*, 3681.

[23] D. F. Liu, A. J. Liang, E. K. Liu, Q. N. Xu, Y. W. Li, C. Chen, D. Pei, W. J. Shi, S. K. Mo, P. Dudin, T. Kim, C. Cacho, G. Li, Y. Sun, L. X. Yang, Z. K. Liu, S. S. P. Parkin, C. Felser, Y. L. Chen, *Science* **2019**, *365*, 1282.

[24] N. Morali, R. Batabyal, P. K. Nag, E. Liu, Q. Xu, Y. Sun, B. Yan, C. Felser, N. Avraham, H. Beidenkopf, *Science* **2019**, *365*, 1286.

[25] S. N. Guin, P. Vir, Y. Zhang, N. Kumar, S. J. Watzman, C. Fu, E. Liu, K. Manna, W. Schnelle, J. Gooth, C. Shekhar, Y. Sun, C. Felser, *Adv. Mater.* **2019**, *31*, 1806622.

[26] L. Ding, J. Koo, L. Xu, X. Li, X. Lu, L. Zhao, Q. Wang, Q. Yin, H. Lei, B. Yan, Z. Zhu, K. Behnia, *Phys. Rev. X* **2019**, *9*, 041061.

[27] S. Howard, L. Jiao, Z. Wang, P. Vir, C. Shekhar, C. Felser, T. Hughes, V. Madhavan, arXiv:1910.11205 **2019**.

[28] L. Muechler, E. Liu, J. Gayles, Q. Xu, C. Felser, Y. Sun, *Phys. Rev. B* **2020**, *101*, 115106.

[29] Y. Okamura, S. Minami, Y. Kato, Y. Fujishiro, Y. Kaneko, J. Ikeda, J. Muramoto, R. Kaneko, K. Ueda, V. Kocsis, N. Kanazawa, Y. Taguchi, T. Koretsune, K. Fujiwara, A. Tsukazaki, R. Arita, Y. Tokura, Y. Takahashi, *Nat. Commun.* **2020**, *11*, 4619.

[30] Y. Xing, J. Shen, H. Chen, L. Huang, Y. Gao, Q. Zheng, Y. Y. Zhang, G. Li, B. Hu, G. Qian, L. Cao, X. Zhang, P. Fan, R. Ma, Q. Wang, Q. Yin, H. Lei, W. Ji, S. Du, H. Yang, W. Wang, C. Shen, X. Lin, E. Liu, B. Shen, Z. Wang, H. J. Gao, *Nat. Commun.* **2020**, *11*, 5613.

[31] Q. Zeng, G. Gu, G. Shi, J. Shen, B. Ding, S. Zhang, X. Xi, C. Felser, Y. Li, E. Liu, *Sci. China Phys. Mech. Astron.* **2021**, *64*, 287512.

[32] C. Liu, J. Shen, J. Gao, C. Yi, D. Liu, T. Xie, L. Yang, S. Danilkin, G. Deng, W. Wang, S. Li, Y. Shi, H. Weng, E. Liu, H. Luo, *Sci. China Phys. Mech. Astron.* **2020**, *64*, 217062.

[33] C. Liu, C. Yi, X. Wang, J. Shen, T. Xie, L. Yang, T. Fennel, U. Stuhr, S. Li, H. Weng, Y. Shi, E. Liu, H. Luo, *Sci. China Phys. Mech. Astron.* **2021**, *64*, 257511.

[34] X. Chen, M. Wang, C. Gu, S. Wang, Y. Zhou, C. An, Y. Zhou, B. Zhang, C. Chen, Y. Yuan, M. Qi, L. Zhang, H. Zhou, J. Zhou, Y. Yao, Z. Yang, *Phys. Rev. B* **2019**, *100*, 165145.

[35] Z. Y. Liu, T. Zhang, S. X. Xu, P. T. Yang, Q. Wang, H. C. Lei, Y. Sui, Y. Uwatoko, B. S. Wang, H. M. Weng, J. P. Sun, J. G. Cheng, *Phys. Rev. Mater.* **2020**, *4*, 044203.

[36] C.-H. Li, Y.-J. Long, L.-X. Zhao, L. Shan, Z.-A. Ren, J.-Z. Zhao, H.-M. Weng, X. Dai, Z. Fang, C. Ren, G.-F. Chen, *Phys. Rev. B* **2017**, *95*, 125417.

[37] P. Vaqueiro, G. G. Sobany, *Solid State Sci.* **2009**, *11*, 513.

[38] W. Schnelle, A. Leithe-Jasper, H. Rosner, F. M. Schappacher, R. Pöttgen, F. Pielnhofer, R. Weihrich, *Phys. Rev. B* **2013**, *88*, 144404.

[39] F. Birch, *Phys. Rev.* **1947**, *71*, 809.

[40] Z. Guguchia, J. A. T. Verezhak, D. J. Gawryluk, S. S. Tsirkin, J. X. Yin, I. Belopolski, H. Zhou, G. Simutis, S. S. Zhang, T. A. Cochran, G. Chang, E. Pomjakushina, L. Keller, Z. Skrzeczkowska, Q. Wang, H. C. Lei, R. Khasanov, A. Amato, S. Jia, T. Neupert, H. Luetkens, M. Z. Hasan, *Nat. Commun.* **2020**, *11*, 559.

[41] J. M. Santiago, C. L. Huang, E. Morosan, *J. Phys.: Condens. Matter* **2017**, *29*, 373002.

[42] J. M. Ziman, *Electrons and Phonons: Theory of Transport Phenomena in Solids*, Oxford University Press, Oxford **1960**.

[43] G. Eguchi, K. Kuroda, K. Shirai, Y. Ando, T. Shinjo, A. Kimura, M. Shiraishi, *Phys. Rev. B* **2015**, *91*, 235117.

[44] C. Haas, *Phys. Rev.* **1968**, *168*, 531.

[45] M. A. Kassem, Y. Tabata, T. Waki, H. Nakamura, *Phys. Rev. B* **2017**, *96*, 014429.

[46] A. Sugawara, T. Akashi, M. A. Kassem, Y. Tabata, T. Waki, H. Nakamura, *Phys. Rev. Mater.* **2019**, *3*, 104421.

[47] D. F. Liu, E. K. Liu, Q. N. Xu, J. L. Shen, Y. W. Li, D. Pei, A. J. Liang, P. Dudin, T. K. Kim, C. Cacho, Y. F. Xu, Y. Sun, L. X. Yang, Z. K. Liu, C. Felser, S. S. P. Parkin, Y. L. Chen, arXiv:2103.08113v1 **2021**.

[48] R. Yang, T. Zhang, L. Zhou, Y. Dai, Z. Liao, H. Weng, X. Qiu, *Phys. Rev. Lett.* **2020**, *124*, 077403.

[49] M. M. Otrokov, I. I. Klimovskikh, H. Bentmann, D. Estyunin, A. Zeugner, Z. S. Aliev, S. Gaß, A. U. B. Wolter, A. V. Koroleva, A. M.

Shikin, M. Blanco-Rey, M. Hoffmann, I. P. Rusinov, A. Y. Vyazovskaya, S. V. Eremeev, Y. M. Koroteev, V. M. Kuznetsov, F. Freyse, J. Sánchez-Barriga, I. R. Amiraslanov, M. B. Babanly, N. T. Mamedov, N. A. Abdullayev, V. N. Zverev, A. Alfonsov, V. Kataev, B. Büchner, E. F. Schwier, S. Kumar, A. Kimura, *et al. Nature* **2019**, *576*, 416.

[50] D. Zhang, M. Shi, T. Zhu, D. Xing, H. Zhang, J. Wang, *Phys. Rev. Lett.* **2019**, *122*, 206401.

[51] J. Li, Y. Li, S. Du, Z. Wang, B.-L. Gu, S.-C. Zhang, K. He, W. Duan, Y. Xu, *Sci. Adv.* **2019**, *5*, eaaw5685.

[52] Y.-J. Hao, P. Liu, Y. Feng, X.-M. Ma, E. F. Schwier, M. Arita, S. Kumar, C. Hu, R. Lu, M. Zeng, Y. Wang, Z. Hao, H.-Y. Sun, K. Zhang, J. Mei, N. Ni, L. Wu, K. Shimada, C. Chen, Q. Liu, C. Liu, *Phys. Rev. X* **2019**, *9*, 041038.

[53] L. J. van der Pauw, *Philips Res. Rep.* **1958**, *13*, 1.

[54] G. Eguchi, S. Paschen, *Phys. Rev. B* **2019**, *99*, 165128.

[55] G. Kresse, J. Furthmüller, *Comput. Mater. Sci.* **1996**, *6*, 15.

[56] G. Kresse, J. Furthmüller, *Phys. Rev. B* **1996**, *54*, 11169.

[57] G. Kresse, D. Joubert, *Phys. Rev. B* **1999**, *59*, 1758.

[58] J. P. Perdew, A. Ruzsinszky, G. I. Csonka, O. A. Vydrov, G. E. Scuseria, L. A. Constantin, X. Zhou, K. Burke, *Phys. Rev. Lett.* **2008**, *100*, 136406.

[59] D. Xiao, M.-C. Chang, Q. Niu, *Rev. Mod. Phys.* **2010**, *82*, 1959.

[60] N. Marzari, D. Vanderbilt, *Phys. Rev. B* **1997**, *56*, 12847.

[61] I. Souza, N. Marzari, D. Vanderbilt, *Phys. Rev. B* **2001**, *65*, 035109.

[62] A. A. Mostofi, J. R. Yates, G. Pizzi, Y.-S. Lee, I. Souza, D. Vanderbilt, N. Marzari, *Comput. Phys. Commun.* **2014**, *185*, 2309.